Dark Matter Limits from Dwarf Spheroidal Galaxies with the HAWC Gamma-Ray Observatory

A. Albert[1], R. Alfaro[2], C. Alvarez[3], J. D. Álvarez[4], R. Arceo[3], J. C. Arteaga-Velázquez[4], D. Avila Rojas[2], H. A. Ayala Solares[5],
N. Bautista-Elivar[6], A. Becerril[2], E. Belmont-Moreno[2], S. Y. BenZvi[7], A. Bernal[8], J. Braun[9], C. Brisbois[5], K. S. Caballero-Mora[3],
T. Capistrán[10], A. Carramiñana[10], S. Casanova[11], M. Castillo[4], U. Cotti[4], J. Cotzomi[12], S. Coutiño de León[10], C. De León[12],
E. De la Fuente[13], R. Diaz Hernandez[10], B. L. Dingus[1], M. A. DuVernois[9], J. C. Díaz-Vélez[13], R. W. Ellsworth[14], K. Engel[15],
D. W. Fiorino[15], N. Fraija[8], J. A. García-González[2], F. Garfias[8], M. M. González[8], J. A. Goodman[15], Z. Hampel-Arias[9],
J. P. Harding[1], S. Hernandez[2], A. Hernandez-Almada[2], B. Hona[5], P. Hüntemeyer[5], A. Iriarte[8], A. Jardin-Blicq[16], V. Joshi[16],
S. Kaufmann[3], D. Kieda[17], R. J. Lauer[18], D. Lennarz[19], H. León Vargas[2], J. T. Linnemann[20], A. L. Longinotti[10],
M. Longo Proper[21], G. Luis Raya[6], R. Luna-García[22], R. López-Coto[16], K. Malone[23], S. S. Marinelli[20], I. Martinez-Castellanos[15],
J. Martínez-Castro[22], H. Martínez-Huerta[24], J. A. Matthews[18], P. Miranda-Romagnoli[25], E. Moreno[12], M. Mostafá[23], L. Nellen[26],
M. Newbold[17], M. U. Nisa[7], R. Noriega-Papaqui[25], R. Pelayo[22], J. Pretz[23], E. G. Pérez-Pérez[6], Z. Ren[18], C. D. Rho[7], C. Rivière[15],
D. Rosa-González[10], M. Rosenberg[23], E. Ruiz-Velasco[2], F. Salesa Greus[11], A. Sandoval[2], M. Schneider[27], H. Schoorlemmer[16],
G. Sinnis[1], A. J. Smith[15], R. W. Springer[17], P. Surajbali[16], I. Taboada[19], O. Tibolla[3], K. Tollefson[20], I. Torres[10], G. Vianello[28],
T. Weisgarber[9], S. Westerhoff[9], J. Wood[9], T. Yapici[20], P. W. Younk[1], and H. Zhou[1]

[1] Physics Division, Los Alamos National Laboratory, Los Alamos, NM, USA; jpharding@lanl.gov
[2] Instituto de Física, Universidad Nacional Autónoma de México, Mexico City, Mexico
[3] Universidad Autónoma de Chiapas, Tuxtla Gutiérrez, Chiapas, Mexico
[4] Universidad Michoacana de San Nicolás de Hidalgo, Morelia, Mexico
[5] Department of Physics, Michigan Technological University, Houghton, MI, USA
[6] Universidad Politecnica de Pachuca, Pachuca, Hidalgo, Mexico
[7] Department of Physics & Astronomy, University of Rochester, Rochester, NY, USA
[8] Instituto de Astronomía, Universidad Nacional Autónoma de México, Mexico City, Mexico
[9] Department of Physics, University of Wisconsin-Madison, Madison, WI, USA
[10] Instituto Nacional de Astrofísica, Óptica y Electrónica, Puebla, Mexico
[11] Instytut Fizyki Jadrowej im Henryka Niewodniczanskiego Polskiej Akademii Nauk, Krakow, Poland
[12] Facultad de Ciencias Físico Matemáticas, Benemérita Universidad Autónoma de Puebla, Puebla, Mexico
[13] Departamento de Física, Centro Universitario de Ciencias Exactase Ingenierias, Universidad de Guadalajara, Guadalajara, Mexico
[14] School of Physics, Astronomy, and Computational Sciences, George Mason University, Fairfax, VA, USA
[15] Department of Physics, University of Maryland, College Park, MD, USA
[16] Max-Planck Institute for Nuclear Physics, D-69117 Heidelberg, Germany
[17] Department of Physics and Astronomy, University of Utah, Salt Lake City, UT, USA
[18] Dept of Physics and Astronomy, University of New Mexico, Albuquerque, NM, USA
[19] School of Physics and Center for Relativistic Astrophysics—Georgia Institute of Technology, Atlanta, GA, USA
[20] Department of Physics and Astronomy, Michigan State University, East Lansing, MI, USA; tyapici@pa.msu.edu
[21] Colorado State University, Physics Dept., Ft Collins, CO, USA; Megan.Longo@colostate.edu
[22] Centro de Investigación en Computación, Instituto Politécnico Nacional, Mexico City, Mexico
[23] Department of Physics, Pennsylvania State University, University Park, PA, USA
[24] Physics Department, Centro de Investigacion y de Estudios Avanzados del IPN, Mexico City, DF, Mexico
[25] Universidad Autónoma del Estado de Hidalgo, Pachuca, Mexico
[26] Instituto de Ciencias Nucleares, Universidad Nacional Autónoma de Mexico, Mexico City, Mexico
[27] Santa Cruz Institute for Particle Physics, University of California, Santa Cruz, Santa Cruz, CA, USA
[28] Department of Physics, Stanford University: Stanford, CA, USA

Abstract

The High Altitude Water Cherenkov (HAWC) gamma-ray observatory is a wide field of view observatory sensitive to 500 GeV–100 TeV gamma-rays and cosmic rays. It can also perform diverse indirect searches for dark matter annihilation and decay. Among the most promising targets for the indirect detection of dark matter are dwarf spheroidal galaxies. These objects are expected to have few astrophysical sources of gamma-rays but high dark matter content, making them ideal candidates for an indirect dark matter detection with gamma-rays. Here we present individual limits on the annihilation cross section and decay lifetime for 15 dwarf spheroidal galaxies within the field of view, as well as their combined limit. These are the first limits on the annihilation cross section and decay lifetime using data collected with HAWC. We also present the HAWC flux upper limits of the 15 dwarf spheroidal galaxies in half-decade energy bins.

Key words: dark matter – galaxies: dwarf – gamma rays: general

1. Introduction

While the evidence for dark matter (DM) is ample, there remains the question of its composition. There are numerous DM candidates, categorized into non-baryonic and baryonic DM. Among the possibilities of the non-baryonic DM candidates, weakly interacting massive particles (WIMPs) are among the leading hypothetical particle physics candidates for cold DM. DM may consist of WIMPs that have fallen out of thermal equilibrium with the hot dense plasma during the beginning of the universe and interact with the known standard

model particles via a force similar in strength to the weak force (Jungman et al. 1996). In dense DM regions, WIMPs can annihilate into standard model particles. The products of the annihilation can produce photons via pion decay, radiative processes by charged leptons, or direct production of gamma-rays through loop processes.

The expected DM annihilation cross-section depends on the exact model of the DM. One popular model is thermal DM in which the DM is produced thermally in the early universe (Berlin et al. 2016). For a thermal relic WIMP, a velocity-weighted cross-section of $\langle \sigma_A v \rangle \cong 3 \times 10^{-26}$ cm^3 s^{-1} in the early universe is needed in order to produce the DM density observed today. However, the kinematics of the DM today are very different than in the early universe. If the DM couples to gauge bosons, this can create a resonance which is amplified for low-velocity DM and significantly increases the DM cross-section with respect to a thermal relic, a process referred to as Sommerfeld enhancement (Lattanzi & Silk 2009; Feng et al. 2010). Due to Sommerfeld enhancement, a cross-section $\langle \sigma_A v \rangle$ can be several orders of magnitude larger today compared to a cross-section of $\langle \sigma_A v \rangle$ in the early universe. In addition to the Sommerfeld enhancement, other theoretical models predict large DM cross-sections, particularly at masses $\gtrsim 10$ TeV. DM bound states, for example, can increase the DM cross-section to even higher cross-sections than the Sommerfeld enhancement, approaching $\langle \sigma_A v \rangle \sim 10^{-22}$ cm^3 s^{-1} (An et al. 2016).

In the TeV–PeV mass range, there has also been recent excitement about decaying DM. WIMP-like particles which decay may be responsible for the observation of an astrophysical neutrino excess by the IceCube detector (Aartsen et al. 2013a, 2013b; Bai et al. 2016; Esmaili & Serpico 2013). These particles could have large DM decay lifetimes and would produce gamma-rays in similar quantity and energy to the observed neutrinos, from 100 TeV to several PeV (Boucenna et al. 2015; Kopp et al. 2015). The gamma-ray searches for this DM, such as those in this paper, will provide additional information on these possible high-flux, high-mass DM signals.

While there are many promising places in the universe to look for signatures of DM, dwarf spheroidal galaxies (dSphs) are among the best candidates for a DM search. They are expected to be extremely DM rich, as gravitational effect studies indicate much more mass present than the luminous material can account for. The dSphs considered in this analysis are companion galaxies of the Milky Way, in what is known as our Local Group. They are very low luminosity galaxies, with low diffuse Galactic gamma-ray foregrounds and little to no astrophysical gamma-ray production (Baring et al. 2016). For these reasons, dSphs can be used to probe the particle nature of DM (such as annihilation cross-section and decay lifetime).

While there are numerous dSphs near the Milky Way, a total of 15 are considered in this analysis: Bootes I, Canes Venatici I, Canes Venatici II, Coma Berenices, Draco, Hercules, Leo I, Leo II, Leo IV, Segue 1, Sextans, Ursa Major I, Ursa Major II, Ursa Minor, and Triangulum II. These dSphs were chosen for their favorable declination angle for the High Altitude Water Cherenkov (HAWC) observatory and well studied DM content.

In this paper, we calculate the expected gamma-ray flux due to annihilation and decay of DM for five channels. We search for DM gamma-ray signatures from the 15 dSphs. Because no significant gamma-ray excess is observed, we report the corresponding upper limits for the annihilation cross-section and lower limits for the decay lifetime for the 15 dSphs based

on the calculated expected flux. In Section 2, we briefly describe the HAWC Observatory. In Section 3, we present the calculation of the expected gamma-ray flux due to DM annihilation or decay. The method for calculating limits is explained in Section 4.1; Appendix A elaborates the method in more detail. In Sections 4 and 5, we discuss the results and compare with other experimental results. We also provide a dedicated section (Appendix B) for interpreting the HAWC flux limits tabulated in the paper.

2. HAWC Observatory

The HAWC observatory detects high-energy gamma-rays and is located at Sierra Negra, Mexico. The site is 4100 m above sea level, at latitude $18°59\rlap{.}'7$ N and longitude $97°18\rlap{.}'6$ W. HAWC is a survey instrument that is sensitive to gamma-rays of 500 GeV to a few hundred TeV (Abeysekara et al. 2017) energies. HAWC consists of 300 water Cherenkov detectors (WCDs) covering 22,000 m^2 area. Each detector contains four photomultiplier tubes (PMTs) (Abeysekara et al. 2017). It has been operating with a partial detector since 2013 August and with the full detector since 2015 March. Here we present results from 507 days of its operations, from 2014 November to 2016 June, analyzed with the Pass 4.1 HAWC reconstruction parameters.

2.1. HAWC Analysis

When an air shower is formed from a cosmic particle hitting the atmosphere, the shower particles impinge on the HAWC WCDs and produce Cherenkov light, which is observed by the PMTs in the WCD. The fraction of the HAWC WCDs hit by an air shower is stored as the variable f_{hit}, which determines the size of the air shower and is used in the estimation of the cosmic particle's energy. Through relative timing of the 300 WCDs, one can determine the direction from which the initial cosmic particle arrived. The type of cosmic particle (hadron or gamma) is determined based on the distribution of the energy deposited in the WCDs across the array. A gamma-ray shower typically has a smoother distribution across WCDs whereas a hadron shower has a clumped distribution, which is used to distinguish gammas from hadrons. To estimate the background at any location on the sky, a technique called "direct integration" is used, as detailed in Abdo et al. (2012).

To analyze spectra, as we do in this paper, HAWC uses a forward-folding technique. A given input spectrum is run through the HAWC detector response as determined through Monte Carlo simulations. This yields an expected gamma-ray event distribution in f_{hit} for that spectrum. This distribution in f_{hit} is compared to the observed event distribution for that location on the sky and the direct integration background event distribution. The statistical techniques for doing this, as well as the uncertainties in this analysis, are detailed in Sections 4.1 and 4.2. Further details about the HAWC analysis are provided in Abeysekara et al. (2017).

3. Dark Matter Gamma-ray Flux

3.1. Gamma-ray Flux from Dark Matter Annihilation

A calculation of the expected gamma-ray flux from DM annihilation requires information about both the astrophysical properties of the potential DM source and the particle properties of the initial- and final-state particles. The

differential gamma-ray flux integrated over the solid angle of the source is

$$\frac{dF}{dE}\bigg|_{\text{annihilation}} = \frac{\langle \sigma_A v \rangle}{8\pi M_\chi^2} \frac{dN_\gamma}{dE} J \qquad (1)$$

where $\langle \sigma_A v \rangle$ is the velocity-weighted DM annihilation cross-section, dN_γ/dE is the gamma-ray spectrum per DM annihilation, and M_χ is the DM particle mass. The J-factor (J) is defined as the dark mass density (ρ) squared and integrated along the line-of-sight distance x and over the solid angle of the observation region

$$J = \int_{\text{source}} d\Omega \int dx \rho^2(r(\theta, x)) \qquad (2)$$

where the distance from the Earth to a point within the source is given by

$$r(\theta, x) = \sqrt{R^2 - 2xR\cos(\theta) + x^2}, \qquad (3)$$

R is the distance to the center of the source, and θ is the angle between the center of the source and the line of sight.

3.2. Gamma-ray Flux from Dark Matter Decay

The gamma-ray flux from DM decay is similar to the DM annihilation gamma-ray flux as described in Equation (1). The decay flux depends on the inverse of the DM lifetime τ instead of the annihilation cross-section:

$$\frac{dF}{dE}\bigg|_{\text{decay}} = \frac{1}{4\pi\tau M_\chi} \frac{dN_\gamma}{dE} D. \qquad (4)$$

Because decays involve only one particle, not two, the gamma-ray flux from DM decay depends on a single power of the DM density ρ instead of the square. This results in a D-factor for decay which differs from the annihilation J-factor and is given by

$$D = \int_{\text{source}} d\Omega \int dx \rho(r_{\text{gal}}(\theta, x)). \qquad (5)$$

Moreover, the total center of mass energy for each DM decay contains only half of the energy as an annihilation of two DM particles of similar masses.

3.3. Dark Matter Density Distributions

The density profiles describe how the density (ρ) of a spherical system varies with distance (r) from its center. In this paper, the Navarro–Frenk–White (NFW) model is used for the DM density profiles. The NFW profile (Navarro et al. 1997, 2009) is the simplest model consistent with N-body simulations. The NFW density profile is given by

$$\rho_{\text{NFW}}(r) = \frac{\rho_s}{(r/r_s)^\gamma (1 + (r/r_s)^\alpha)^{(\beta-\alpha)/\gamma}} \qquad (6)$$

where ρ_s is the scale density, r_s is the scale radius of the galaxy, γ is the slope for $r \ll r_s$, β is the slope for $r \gg r_s$ and α is the transition parameter from inner slope to outer slope. The source parameter values for the 15 dSphs presented are listed in Table 1. The J-factor and D-factor for each source are calculated by the CLUMPY software (Bonnivard et al. 2016) using different realizations of the tabulated values and their respective uncertainties for an angular window of

θ_{max}. The median values for each source are given in Table 1. For Triangulum II, these calculations were not performed due to the fact that the parameter set needed for the calculations is not given in the literature, so we use J- and D-factors from Hayashi et al. (2016).

3.4. Dark Matter Gamma-ray Spectra

The PYTHIA program models interactions between two incoming particles and their outgoing particles (Sjöstrand et al. 2006). This makes the program ideal for simulating interactions between two DM particles and monitoring the number of gamma-rays we expect to see as a result of the DM annihilation. PYTHIA 8.2 (Sjöstrand et al. 2015) was used in this analysis to calculate the expected photon spectrum for each WIMP annihilation channel. The photon radiation of charged particles was simulated, as well as the decay of particles such as the π^0 (Abeysekara et al. 2014; Harding 2015). For each annihilation channel and each DM mass, the average number of photons in energy bins per annihilation event was calculated. This differential flux, dN_γ/dE, was used to determine the DM gamma-ray flux of the targeted source.

Due to the available phase space, DM will usually annihilate into the heaviest available channel, so we consider the heavy top quark ($t\bar{t}$) and tau lepton ($\tau^+\tau^-$) channels. The bottom quark channel ($b\bar{b}$) is included since it has been studied by several experiments (Fermi-LAT, MAGIC, etc.) to allow for direct comparison of results. The W-channel (W^+W^-) was chosen since it is a standard bosonic channel that is widely considered in other experiments. Finally the muon channel ($\mu^+\mu^-$) is included in this analysis since DM models which are dominated by annihilation into light leptons may be able to explain measured excesses of local positrons (Cholis et al. 2009). For DM decay, the same channels are used.

An example of the generated expected gamma-ray flux is shown in Figure 1 for DM of mass 1 TeV and 108 TeV annihilating into $b\bar{b}$ and $\tau\tau$. In this work, we scanned DM masses from 1 TeV up to 100 TeV.

4. Limits on the Dark Matter Annihilation Cross Section and Decay Lifetime with HAWC Data

In this section, we present the individual and combined limits from 15 dSphs within the HAWC field of view for the HAWC 507 day data. To put the limits in a proper statistical context, we also discuss the statistical methods for calculating limits, the systematic uncertainties on the limits, and the flux limits we calculate from the data.

The limits were calculated assuming that the dSphs are point sources, since the angular resolution of the HAWC observatory ($\sim 0°.5$) (Abeysekara et al. 2017) is larger than the typical dSph scale radius. The significance of the expected gamma-ray flux for a range of DM masses, 1–100 TeV, and five DM annihilation channels was calculated as described in Section 4.1. In Figure 2, we show the significance of DM annihilation into the selected channels. We assign $-\sqrt{\text{TS}}$ for significance instead of $\sqrt{\text{TS}}$ if the best fit yields a gamma-ray deficit.

Since no significant gamma-ray excess was observed, 95% confidence level limits were placed on the annihilation cross-section and decay lifetime using the method described in Section 4.1. The source significance is used to determine the exclusion curves on the DM annihilation cross-section $\langle \sigma_A v \rangle$

Table 1
Astrophysical Parameters and *J*- and *D*-factors, for the Fifteen dSphs within the HAWC Field of View

Source	R.A. (degree)	Decl. (degree)	R (kpc)	$\log_{10}(\rho_s/M_\odot/\mathrm{pc}^3)$	$\log_{10}(r_s/\mathrm{pc})$	θ_{max} (degree)	α	β	γ	$\log_{10}(J/\mathrm{GeV}^2\,\mathrm{cm}^{-5}\,\mathrm{sr})$	$\log_{10}(D/\mathrm{GeV}\,\mathrm{cm}^{-2}\,\mathrm{sr})$	$\sqrt{\mathrm{TS}}$ (σ)
Bootes 1	210.05	14.49	66	−1.74	3.80	0.47	1.96	5.91	0.53	18.47	18.45	−0.43
Canes Venatici I	202.04	33.57	218	−1.87	3.36	0.53	1.86	6.00	0.67	17.62	17.55	−0.11
Canes Venatici II	194.29	34.32	160	−1.46	3.91	0.13	1.92	6.09	0.43	17.95	17.68	−0.50
Coma Berenices	186.74	23.90	44	−0.99	3.71	0.31	1.99	6.44	0.43	19.32	18.71	−1.35
Draco	260.05	57.07	76	−1.74	3.57	1.30	2.01	6.34	0.71	19.37	19.15	0.37
Hercules	247.72	12.75	132	−1.62	2.93	0.28	1.81	6.39	0.55	16.93	16.87	−1.05
Leo I	152.11	12.29	254	−2.18	3.80	0.45	1.93	6.15	0.84	17.57	18.04	−0.40
Leo II	168.34	22.13	233	−0.92	2.89	0.23	1.76	5.95	0.82	18.11	17.33	0.17
Leo IV	173.21	−0.53	154	−1.80	2.94	0.16	1.93	6.32	0.55	16.37	16.50	−0.16
Segue 1	151.75	16.06	23	−1.06	3.26	0.35	1.91	6.39	0.76	19.66	18.64	−0.13
Sextans	153.28	−1.59	86	−2.39	3.79	1.70	1.98	6.06	0.63	17.96	18.59	0.43
Triangulum II	33.32	36.18	30	...	...	...	...	...	...	20.44	18.42	−0.46
Ursa Major I	158.72	51.94	97	−1.84	3.50	0.53	1.87	6.25	0.71	18.66	18.11	−0.03
Ursa Major II	132.77	63.11	32	−1.13	3.63	0.43	1.86	6.37	0.58	19.67	19.05	0.32
Ursa Minor	227.24	67.24	76	−0.50	2.60	1.37	1.64	5.29	0.78	19.24	17.92	−0.30

Note. The source, right ascension (R.A.), declination (decl.), scale density (ρ_s), scale radius (r_s), distance to the source (R), and the DM *J*-factor and *D*-factor are listed above. NFW profiles parameters from Geringer-Sameth et al. (2015) are used for all sources listed, except for Triangulum II. For Triangulum II, we use the *J*- and *D*-factor from Hayashi et al. (2016). *J*- and *D*-factors are calculated for integration angle of θ_{max} for respective sources. The significance (σ) is also shown for each source for $M_\chi = 12$ TeV and the $\chi\chi \to \tau^+\tau^-$ annihilation channel.
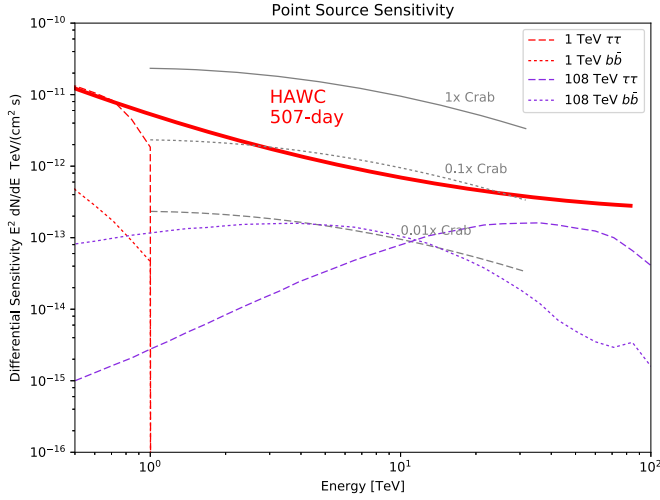
Figure 1. Expected gamma-ray flux from annihilation into two separate channels ($\tau\tau$ and $b\bar{b}$) of 1 TeV and 108 TeV DM compared with HAWC point source sensitivity. The J-factor of Segue 1, $J = 10^{19.66}$ GeV^2 cm^{-5} sr, and $\langle\sigma v\rangle = 10^{-23}$ cm^3 s^{-1} are used for the calculation of the expected fluxes.

and decay lifetime τ, for the individual dSphs. A joint likelihood analysis was also completed by combining the statistics for all 15 dSphs in order to increase the sensitivity of the analysis.

Triangulum II has a particularly large J-factor and transits near the zenith for HAWC. However, this dSph was only discovered recently (Laevens et al. 2015) and still has large uncertainties in its mass profile. Because of this, we show the joint dSph limit both including and excluding Triangulum II in Figures 3–5.

It should be noted that the ability to include data collected on a dSph which was newly discovered since the beginning of the experiment is a strength of the HAWC design. With the HAWC wide field of view and large uptime, data for all declinations within the HAWC field of view exist, so further dSphs can be added to this analysis once their position and DM content are known.

4.1. Calculation of Limits on the Dark Matter Annihilation Cross-section and Decay Lifetime

To quantify the gamma-ray excess in a particular region of the sky, we perform a likelihood ratio test. This allows us to calculate the significance of a source that has a low signal-to-noise ratio (Neyman & Pearson 1933). For each dSph, DM mass, DM channel, and both annihilation and decay, the corresponding gamma-ray flux from Section 3 is forward-folded through the HAWC analysis chain to calculate its expected $f_{\rm hit}$ distribution. A likelihood test is performed on this distribution combined with the background $f_{\rm hit}$ distribution from direct integration versus the $f_{\rm hit}$ distribution measured by HAWC. An analysis is also performed in which all 15 dSphs considered are included in a single joint likelihood test.

For the likelihood of the signal region $\mathcal{L}$ and the likelihood of the background region $\mathcal{L}_0$, we calculate the test statistic

$$\text{TS} = -2\ln\left(\frac{\mathcal{L}_0}{\mathcal{L}(S_{\max})}\right) \tag{7}$$

where $S_{\max}$ is the value of signal flux which maximizes the likelihood. The factor of two in the definition of the test statistic

causes the distribution of TS values to asymptotically approach a χ^2 distribution (Wilks 1938).

For a χ^2-distributed TS, the process for setting 95% CL limits consists of finding S_{95}, the amount of signal which would change the value of $-2\ln(\mathcal{L}_0/\mathcal{L})$ by 2.71, that is

$$\text{TS} + 2\ln\left(\frac{\mathcal{L}_0}{\mathcal{L}(S_{95})}\right) = 2.71. \tag{8}$$

It was noted by Protassov et al. (2002) that near parameter boundaries (such as upper limits) the likelihood ratio test does not perfectly match a χ^2 distribution, so numerical calculations are preferred. However, the method above is one typically used in particle astrophysics (Patrignani et al. 2016). Furthermore, the limits we compare to from other experiments, e.g., those from Ackermann et al. (2014), use this method, so we follow it in this work to allow our limits to be directly compared to those of other astrophysics experiments.

We see little to no gamma-ray signal coming from the direction of the dSphs. This can be seen in the sample significances given in Table 1 and the plots in Figure 2. However, if the value of $S_{\max}$ is unphysical, i.e., $S_{\max} < 0$, we set $\mathcal{L}(S_{\max}) = \mathcal{L}_0$ so that TS is replaced by $-2\ln(\mathcal{L}_0/\mathcal{L}(S_{\max})) = 0$ and instead and we find S_{95} by

$$2\ln\left(\frac{\mathcal{L}_0}{\mathcal{L}(S_{95})}\right) = 2.71. \tag{9}$$

After having determined the allowed amount of signal flux at 95% CL, we solve Equation (1) or Equation (4) to find the corresponding values $\langle\sigma_A v\rangle_{95}$ or τ_{95} which produce that flux.

The joint likelihood analysis is a stacked study of many dSphs. A combined analysis increases the overall statistical power and produces a better constraint on the DM annihilation cross-section and decay lifetime. The same likelihood analysis procedure is followed as described in the above section. However, the likelihood values are instead summed over all sources rather than over a single source. For a more detailed discussion of the limit-setting procedure, see Appendix A.

4.2. Systematics

Systematic uncertainties arise from a number of sources within the detector, for example the uncertainties associated from taking data at different stages of the detector. Since HAWC was operational during its construction, there are data uncertainties due to the changing number of online WCDs and PMTs, the effects of which were studied using different simulations assuming a different number of PMTs. This effect is minimal considering the data set used in the analysis, but it is included in the systematic uncertainties. In addition, the difference among signal efficiencies was compared for simulations varying detector parameters within their systematic errors (Abeysekara et al. 2017). Another uncertainty comes from the measured number of photoelectrons, based on how well we simulate the detector, since muon studies have shown there is a discrepancy between the simulated PMT charge and the charge from actual data. There is also an uncertainty associated with the angular resolution of HAWC. Also, relative PMT photon detection efficiency and charge resolution vary from PMT to PMT. With these effects taken into consideration, Abeysekara et al. (2017) found that this gives an overall systematic uncertainty on the HAWC data set on the order of $\pm 50\%$ on the observed flux. The uncertainties on the
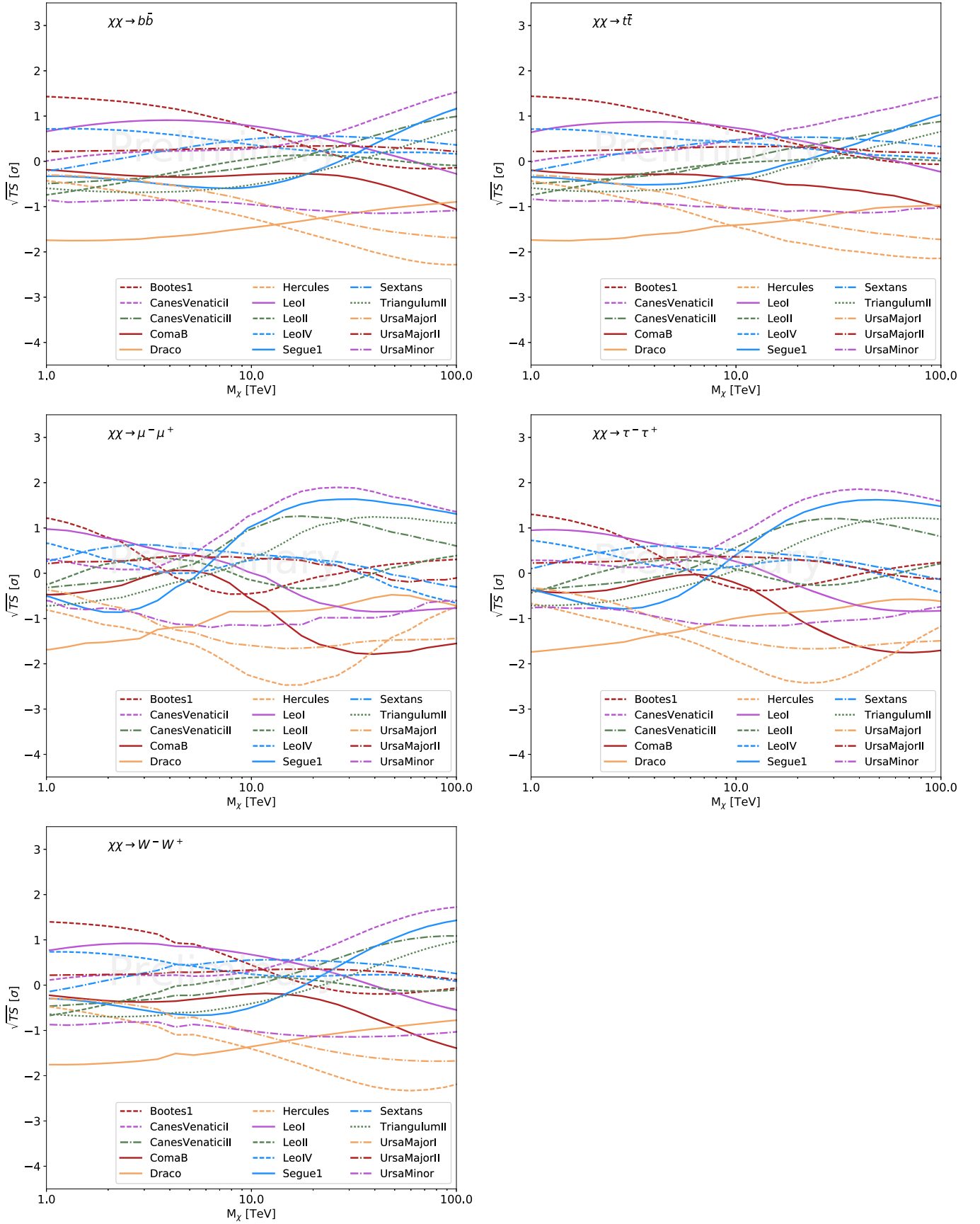
Figure 2. Statistical significance of DM annihilating into $b\bar{b}$, $t\bar{t}$, $\mu^-\mu^+$, $\tau^-\tau^+$ and W^-W^+ channels for the selected sources.
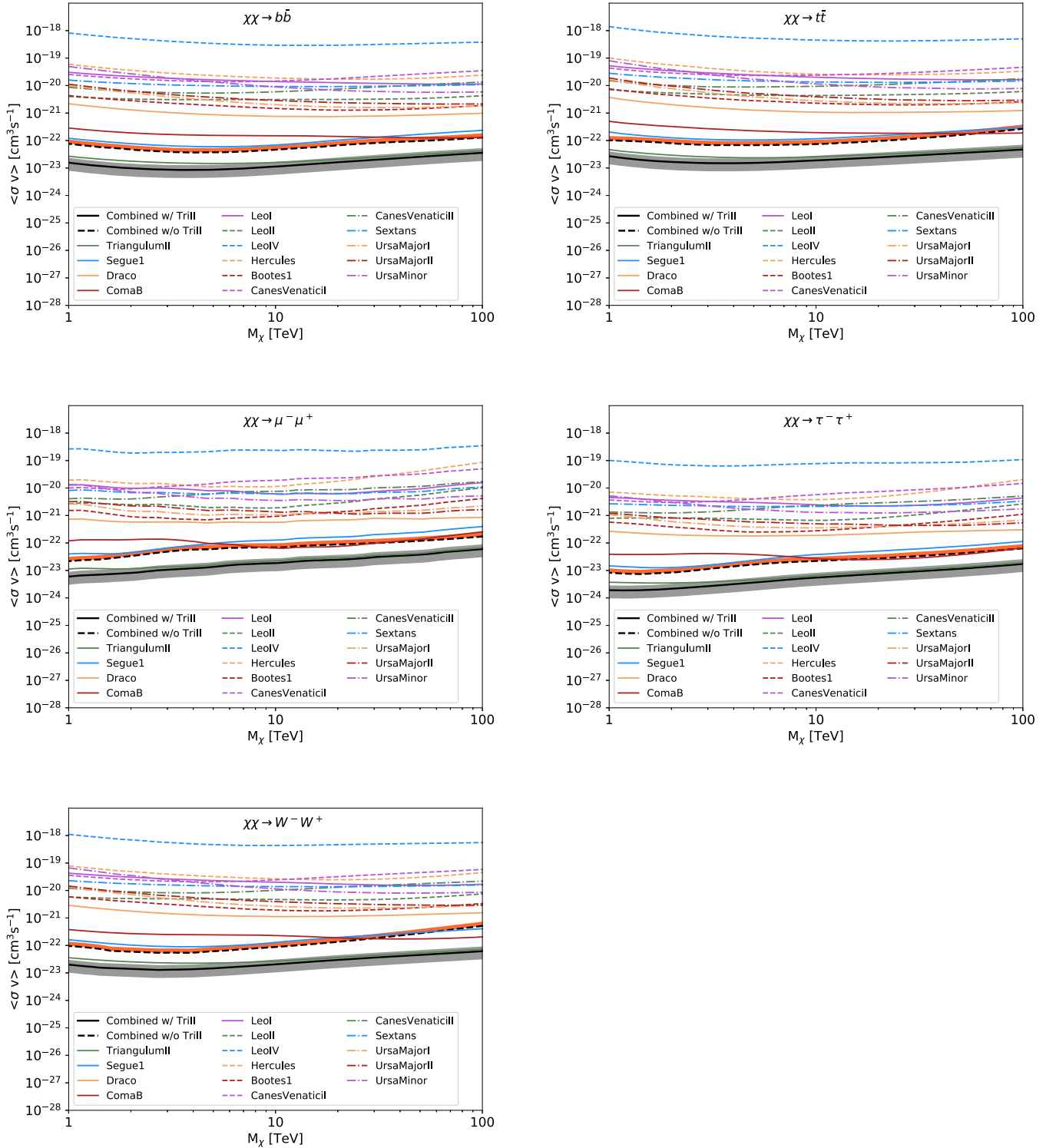
Figure 3. 95% confidence level upper limits on the DM annihilation cross-section for 15 dSphs within the HAWC field of view for the $b\bar{b}$, $t\bar{t}$, $\tau^+\tau^-$, $\mu^+\mu^-$ and W^+W^- annihilation channels. The solid black line shows the combined limit using all dSphs resulting from a joint likelihood analysis. The dashed black line shows the combined limit using 14 dSphs, excluding Triangulum II. The gray band shows the systematic uncertainty on the combined limits due to HAWC systematics and the dark orange band shows the systematic uncertainty due to J-factor uncertainty.

expected DM annihilation and decay limits were calculated to account for these systematic uncertainties.

There are also systematic uncertainties on the expected DM flux due to the integration angle of the J- and D-factors. These uncertainties are different from those of the J- and D-factors due to kinematic modeling of the source. HAWC's angular

resolution changes between $1°$ and $0.2°$ for near-zenith angles. For better angular resolution, the integration angle gets smaller, which results in smaller J- and D-factors. Similarly, for worse angular resolution, the integration angle gives larger values. However, there is a physical constraint on the DM distribution which limits the DM content of a source at angles
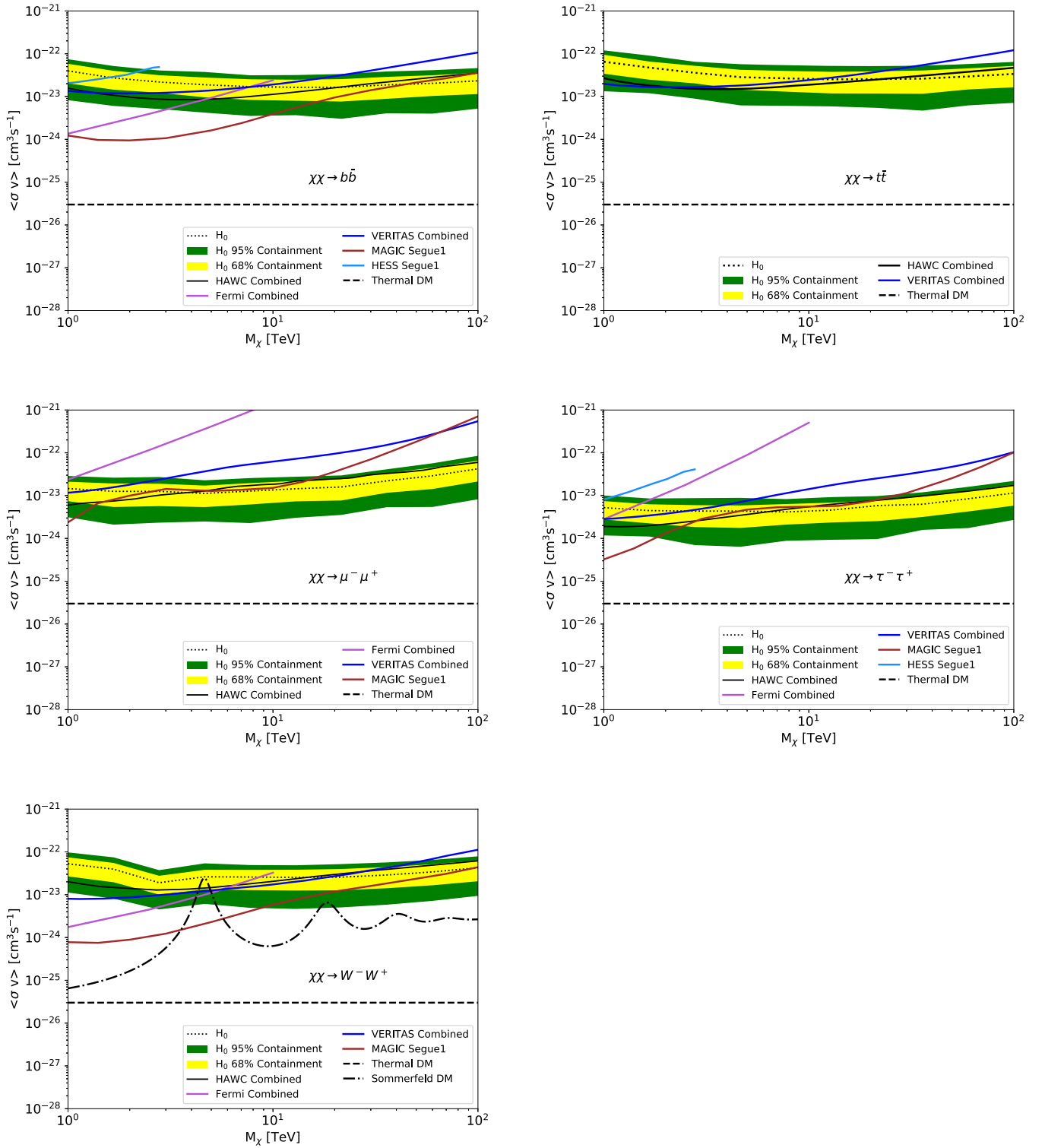
Figure 4. 95% confidence level upper limits on the DM annihilation cross-section for the five DM annihilation channels considered in this analysis and their comparison of the DM annihilation cross-section limits of HAWC to other experimental results for the $b\bar{b}$, $t\bar{t}$, $\tau^+\tau^-$, $\mu^+\mu^-$ and W^+W^- annihilation channels. The HAWC 507 day limits from data are shown by the black solid line. The dashed black line shows the combined limit using 14 dSphs, excluding Triangulum II. *Fermi*-LAT combined dSph limits (Ackermann et al. 2014), VERITAS Segue 1 limits (Archambault et al. 2017), HESS combined dSph limits (Abramowski et al. 2014), and MAGIC Segue 1 limits (Ahnen et al. 2016) are shown for comparison. The same color scheme is used for all the experiment comparison plots.

larger than θ_{max}, where the DM halo is assumed to end. We impose this physically motivated constraint on the J- and D-factor uncertainty calculations, resulting in a one-side uncertainty. For the combined limit uncertainties, we use the uncertainties corresponding to Segue 1 (42% for annihilation cross-section limits and 38% for decay lifetime limits) since it is one of the strongest sources that is driving the limits. Though it would have been better to calculate and use these uncertainties for Triangulum II, the required information is not yet available.
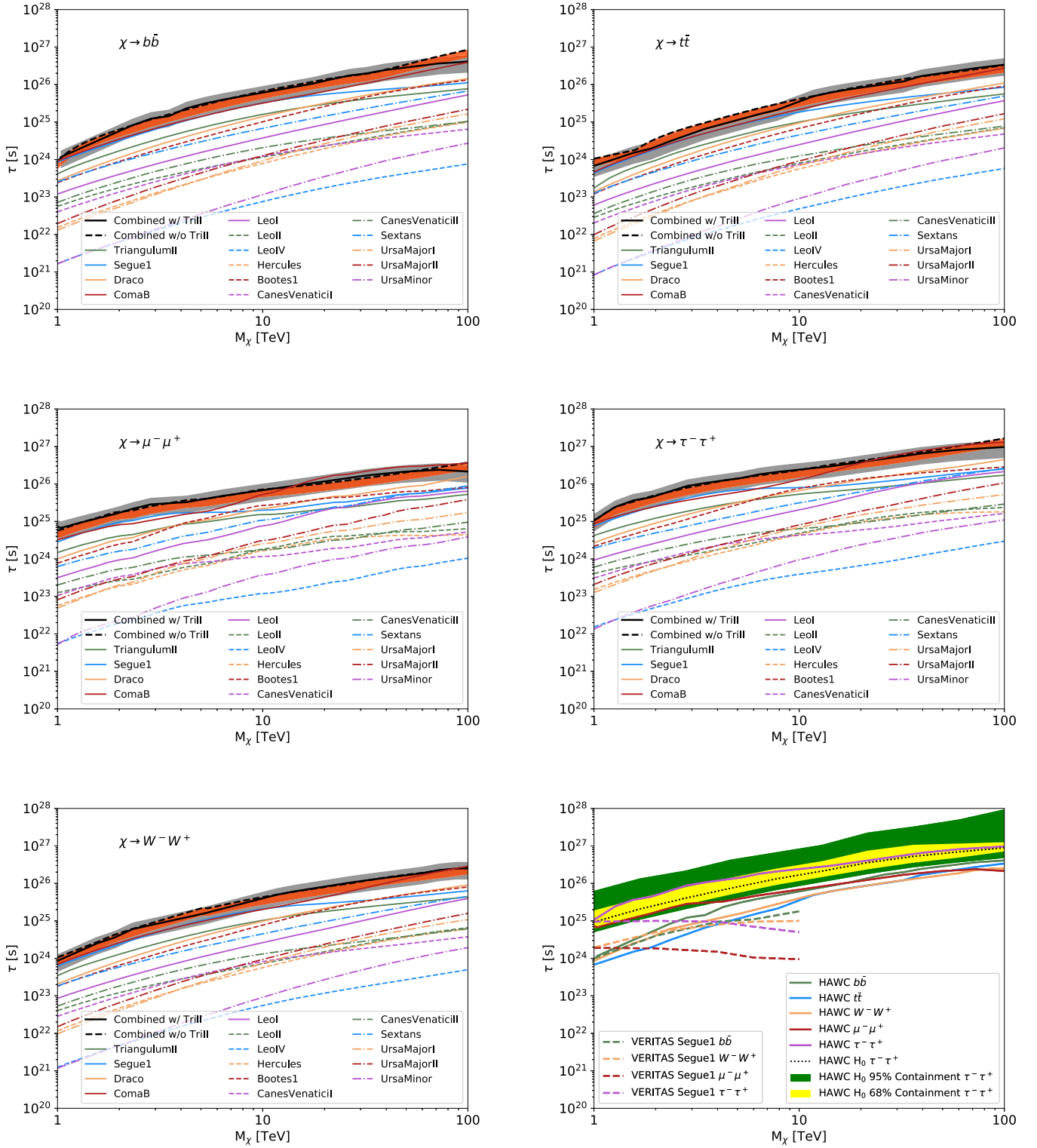
Figure 5. 95% CL lower limits on the DM decay lifetime for 15 dSphs within the HAWC field of view for the $b\bar{b}$, $t\bar{t}$, $\tau^+\tau^-$, $\mu^+\mu^-$ and W^+W^- decay channels. The individual limits are shown from the likelihood analysis for all 15 dSphs with the colored dashed and solid lines. The solid black line shows the combined limit using these 15 dSphs resulting from a joint likelihood analysis. The gray band shows the systematic uncertainty on the combined limits. The dashed black line shows the combined limit using 14 dSphs resulting from a joint likelihood analysis, excluding Triangulum II. The gray band shows the systematic uncertainty on the combined limits due to HAWC systematics and the dark orange band shows the systematic uncertainty due to D-factor uncertainty. Combined limits for different channels are compared with VERITAS Segue 1 limits (Aliu et al. 2012) in the bottom right panel.

4.3. Flux Upper Limits

The annihilation cross-section and decay lifetime results depend on the DM annihilation or decay gamma-ray spectra used for the sources. A quasi-model-independent upper flux limit for each source can be calculated to provide data for testing other models, following the same method outlined by Aartsen et al. (2017). We calculated flux limits separately for five energy bins with width $0.5\log(E/\text{TeV})$ centered at 1 TeV,

Table 2
Quasi-model-independent Best-fit Flux Values and Single-bin 95% Upper Flux Limits Calculated for Fifteen dSphs

Source	0.56–1.78 TeV [10^{-12} TeV^{-1} cm^{-2} s^{-1}]	1.78–5.62 TeV [10^{-14} TeV^{-1} cm^{-2} s^{-1}]	5.62–17.78 TeV [10^{-15} TeV^{-1} cm^{-2} s^{-1}]	17.78–56.23 TeV [10^{-16} TeV^{-1} cm^{-2} s^{-1}]	>56.23 TeV [10^{-17} TeV^{-1} cm^{-2} s^{-1}]
Bootes 1	1.06 ± 1.29 (3.19)	-1.66 ± 3.90 (5.02)	-0.23 ± 1.43 (2.24)	0.25 ± 0.80 (1.67)	0.29 ± 0.70 (1.56)
Canes Venatici I	0.23 ± 1.63 (2.92)	3.09 ± 4.68 (10.8)	3.44 ± 1.88 (6.61)	1.44 ± 1.00 (3.18)	0.75 ± 0.80 (2.18)
Canes Venatici II	-0.38 ± 1.72 (2.47)	1.02 ± 4.92 (9.18)	2.13 ± 1.92 (5.37)	0.52 ± 0.99 (2.25)	0.08 ± 0.75 (1.45)
Coma Berenices	-0.54 ± 1.26 (1.61)	0.07 ± 3.81 (6.39)	-2.19 ± 1.36 (1.08)	-1.36 ± 0.77 (0.62)	-0.79 ± 0.66 (0.69)
Draco	-31.24 ± 18.33 (12.19)	-42.52 ± 36.49 (31.25)	-9.13 ± 11.57 (12.19)	-2.44 ± 4.54 (5.70)	-1.88 ± 2.16 (2.44)
Hercules	-1.63 ± 1.34 (1.11)	-7.01 ± 4.02 (2.70)	-3.65 ± 1.35 (0.78)	-0.75 ± 0.65 (0.70)	-0.15 ± 0.56 (0.93)
Leo I	1.08 ± 1.34 (3.29)	0.92 ± 4.05 (7.64)	-1.13 ± 1.48 (1.67)	-0.71 ± 0.65 (0.74)	-0.43 ± 0.49 (0.65)
Leo II	0.17 ± 1.25 (2.24)	1.00 ± 3.82 (7.34)	-0.67 ± 1.38 (1.80)	0.11 ± 0.74 (1.43)	0.28 ± 0.62 (1.42)
Leo IV	0.79 ± 2.32 (4.60)	-0.39 ± 6.38 (10.18)	0.72 ± 2.48 (4.91)	-0.69 ± 1.19 (1.52)	-0.82 ± 0.73 (0.88)
Segue 1	-1.06 ± 1.26 (1.27)	0.87 ± 3.81 (7.19)	2.51 ± 1.49 (5.06)	1.22 ± 0.88 (2.77)	0.75 ± 0.74 (2.08)
Sextans	1.42 ± 2.53 (5.58)	3.97 ± 6.82 (15.27)	0.92 ± 2.59 (5.30)	-0.06 ± 1.20 (2.05)	-0.36 ± 0.83 (1.23)
Triangulum II	-1.39 ± 1.95 (2.11)	-0.73 ± 5.48 (8.38)	1.74 ± 2.01 (5.15)	1.20 ± 1.01 (2.97)	0.72 ± 0.78 (2.13)
Ursa Major I	-5.01 ± 8.18 (9.35)	-24.09 ± 18.80 (15.22)	-10.41 ± 6.34 (4.48)	-3.42 ± 2.35 (1.98)	-1.82 ± 1.29 (1.23)
Ursa Major II	20.21 ± 75.84 (145.12)	73.04 ± 127.60 (283.45)	19.53 ± 35.24 (77.80)	-0.42 ± 12.96 (21.24)	0.49 ± 5.60 (10.22)
Ursa Minor	-197.86 ± 209.89 (200.62)	-326.40 ± 395.14 (402.60)	-91.40 ± 90.59 (84.10)	-14.96 ± 25.53 (30.44)	-3.87 ± 10.00 (13.78)

Note. The single bin flux limit is given in parentheses after the best-fit flux and its uncertainty. A spectral index of -2 was assumed for evaluating the flux normalization.

3.16 TeV, 10 TeV, 31.6 TeV, and 100 TeV, assuming a flux that is non-zero only within a given interval. 95% confidence limits were calculated for each energy bin assuming the flux is a power law with a spectral index of $\Gamma = -2$. The limits were also tested assuming spectral indices between 0 and -3 to study the spectral index dependence. The flux values calculated for different spectral indices have a variation of $\sim$42% at the lowest-energy bin. The variations get smaller for higher-energy bins, $\sim$25% at the highest-energy bin. These results with different spectral indices are consistent within the systematic HAWC flux uncertainties (Abeysekara et al. 2017).

We report the normalization factors of the power law with spectral index of $\Gamma = -2$ for the upper flux limits in Table 2. For a discussion on using these limits, see Appendix B.

4.4. Dark Matter Annihilation Cross-section Limits

The 95% confidence level upper limits for DM annihilating with 100% branching ratio into the $b\bar{b}$ channel are shown in the first panel of Figure 3. The individual limits are shown for each dSph considered in this analysis. Figure 3 shows 15 individual dSphs as well as the combined limit resulting from a joint likelihood analysis. The systematic uncertainties on the observed flux are shown as gray bands and the systematic uncertainties about the integration angle are shown as orange bands on the combined limits.

The combined limit is dominated by the influence of the three most constraining dSphs with large J-factors and favorable declination for HAWC: Segue 1, Coma Berenices, and Triangulum II. The addition of the remaining twelve dSphs does not significantly change the combined annihilation limits. Despite some of them having relatively large J-factors, they are close to the edge of the field of view of HAWC. Thus, HAWC is not sensitive to these sources. The other panels of Figure 3 show the same information but for DM annihilating with 100% branching ratio into the $\tau^+\tau^-$, $\mu^+\mu^-$, $t\bar{t}$, and W^+W^- channels. Comparisons of these limits to those of other experiments can be seen in Figure 4. The most constraining HAWC limit comes from the $\tau^+\tau^-$ annihilation channel for all DM masses considered here.

We repeated the combined analysis on multiple data sets with the HAWC detected background and Poisson fluctuated signal in order to calculate the expected signal. The results of the repeated analysis is used to calculate the mean expected signal, H_0, as well as 95% and 68% containment of the expected signals.

The combined HAWC limits are compared to limits from four other gamma-ray experiments' observations of dSphs in Figure 4. These are the *Fermi*-LAT combined dSph limits (Ackermann et al. 2014), Veritas Segue 1 limits (Aliu et al. 2012), HESS combined dSph limits (Abramowski et al. 2014), and MAGIC Segue 1 limits (Ahnen et al. 2016).

For the $b\bar{b}$ channel, the MAGIC Segue 1 limit is the most constraining up to $\sim$50 TeV. After $\sim$50 TeV, the HAWC combined dSph limit is the most stringent limit for this channel. Similarly, the MAGIC Segue 1 limit is the most constraining in the mass range we analyzed. It should be noted that Ahnen et al. (2016) reports negative fluctuations for these channels. The HAWC limit is consistent within uncertainties with the Veritas Segue 1 limit. For the leptonic $\mu^+\mu^-$ and $\tau^+\tau^-$ channels, the HAWC combined dSph limits are the strongest above a few TeV.

In Figure 4, DM models for thermal relic and Sommerfeld-enhanced cross-sections are shown for comparison. For the Sommerfeld enhancement, a weak-scale coupling of 1/35 and a very conservative DM velocity of 300 km s^{-1} was assumed. In this work, only the W^+W^- annihilation channel is taken into account for the Sommerfeld enhancement since this channel is assured to have DM coupled to gauge bosons (Feng et al. 2010). At resonances, the HAWC limit rules out a DM with mass of $\sim$4 TeV and the HAWC limit approaches corresponding Sommerfeld-enhanced models by 1 order of magnitude for a DM with mass of $\sim$20 TeV. Slower DM velocity enhances the amplitude of resonances, thus making the HAWC results closer to a Sommerfeld-enhanced thermal relic.

4.5. Dark Matter Decay Lifetime Limits

DM decay lifetime 95% CL lower limits calculated for individual channels (with 100% branching ratio) with 507 day HAWC data are shown in Figure 5. The top, middle, and

bottom panels show the quark channels, lepton channels, and boson channel, respectively, for DM masses ranging from 1–100 TeV. Figure 5 shows 15 individual dSph limits, and the combined limit from these 15 dSphs (in black). Similar to the DM annihilation results, the limits are driven by Segue 1, Coma Berenices, and Triangulum II, though for decays, Bootes I and Draco also contribute significantly to the combined limits. This is due to the fact that DM decay is related to $\int \rho$ (total DM mass) compared to $\int \rho^2$ at the source of annihilation or decay. The *D*-factors of these sources have a different hierarchy of importance than for the *J*-factors for annihilation.

For the lepton channels, due to negative significance at high DM masses, the Coma Berenices limits exhibit an increase; however, as in the annihilation limits, the effect is nullified in the joint likelihood analysis. The strongest overall lower limit is attained by the $\tau^+\tau^-$ channel, which is followed by the other lepton channel ($\mu^+\mu^-$).

5. Summary and Outlook

In this analysis, we searched for DM annihilation and decay signals from 15 dSphs. We observed no significant excess from these sources. Thus, we calculated individual limits for the 15 dSphs within the HAWC field of view using a likelihood ratio analysis method for five DM channels. Combined limits from a joint likelihood analysis of all dSphs were also shown. The combined analysis was done to increase the statistical power of the analysis. These are the first limits on the DM annihilation cross-section and decay lifetime using data collected from the completed HAWC array.

The HAWC combined 15 dSph limits were also compared to four other gamma-ray experiments, *Fermi*-LAT, VERITAS, HESS, and MAGIC. While HAWC annihilation cross-section limits with 507 days of data provide complementary results below a few TeV, HAWC limits are the most constraining limits above 2–3 TeV and above ∼50 TeV for the ($t\bar{t}$, $\mu^-\mu^+$, $\tau^-\tau^+$) and ($b\bar{b}$, W^-W^+) channels, respectively. As for the decay lifetime limits, HAWC has the only limits above 10 TeV and has the most constraining decay lifetime limits with dSph for all channels. HAWC decay lifetime limits provide the only limits at DM masses higher than ∼10 TeV with dSphs.

We are working on improving our analysis tools for enhancing energy and angular resolution. Moreover, an approved extension of HAWC, consisting of smaller tanks around the HAWC array perimeter, is being built. With more data collected and improvements on analysis tools and the detector, HAWC is expected to be more sensitive at lower DM masses, as well as improving its limits at high masses.

In addition to the prompt gamma-ray emission discussed here for the calculations of the limits, the charged particles produced in the annihilation or decay may undergo other physical process (such as inverse Compton scattering and bremsstrahlung) that yield more gamma-rays as the charged particles propagate. The gamma-ray flux due to such phenomena peaks at lower energies than the prompt emission. Thus, the gamma-ray flux spectrum will extend down to much lower energies. For the lepton channels, particularly, this effect can increase the DM gamma-ray flux significantly. Inclusion of these processes may improve the HAWC DM limits. An analysis with these additional physics processes will be conducted in the future.

Appendix A
Detailed Calculation of Limits on the Dark Matter Annihilation Cross-section and Decay Lifetime

For each bin of the analysis, in both f_{hit} and spatial bins, we consider the number of observed signal counts N and the number of observed background counts B. More detail about the background calculations is explained in Abeysekara et al. (2017). The number of expected excess counts from a DM source S can be calculated by convolving Equation (1) with the detector energy response at the source position and the point-spread function. Then, we define twice the log-likelihood ratio (TS) as,

$$\mathrm{TS} = -2 \ln \left(\frac{\mathcal{L}_0}{\mathcal{L}^{\max}} \right) \qquad (10)$$

where $\mathcal{L}_0$ is the null hypothesis (no DM model) likelihood and $\mathcal{L}^{\max}$ is the alternative hypothesis (with DM model) likelihood, evaluated at the value of the cross-section which maximizes the likelihood. Both likelihoods are taken to be Poisson distributions in each bin:

$$\mathcal{L} = \prod_i \frac{(B_i + S_i)^{N_i} \exp[-(B_i + S_i)]}{N_i!} \qquad (11)$$

where S_i is the sum of expected number of signal counts corresponding to a annihilation cross-section or a decay lifetime, B_i is the number of background counts observed, and N_i is the total number of counts observed. Since negative DM cross-sections and lifetimes are physically not allowed, the value of S_i is restricted to positive values. Therefore, for sources which are within underfluctuations of the background, the value of S_i which maximizes the likelihood is $S_i = 0$, consistent with no gamma-rays from DM annihilation or decay. For these underfluctuations, we find

$$\mathcal{L}^{\max} = \mathcal{L}_0 = \prod_i \frac{B_i^{N_i} \exp[-B_i]}{N_i!}. \qquad (12)$$

This gives a TS value of zero for these underfluctuations.

The likelihood is calculated over all spatial bins within 5 degrees of the source and all HAWC analysis bins (f_{hit} bins) (Abeysekara et al. 2017). The spatial binning we use in this analysis spans $0.0573°$ corresponding to 9.986×10^{-7} sr, smaller than the point-spread function of the detector. Also,

because the DM profile peaks strongly toward the center of each source, as discussed in Section 3.3, much faster than the HAWC point-spread function, we expect negligible difference between a point-source analysis and one treating the dSphs as extended sources.

A.1. 95% Confidence Level Limit Calculation

Although the null hypothesis is a good approximation for our sources, we have set up our likelihood calculation to be robust to possible statistical fluctuations or small positive indications of sources. The TS corresponds to an annihilation cross-section, $\langle \sigma_A v \rangle_{\mathrm{max}}$ or decay lifetime, τ_{max}; however the subscripts for cross-section and lifetime should not be interpreted as their maximum values. In the case of the dSphs, TS is zero or very close to zero.

We calculate an upper limit on the annihilation cross-section or a lower limit on the decay lifetime by setting the 95% CL limit. The log-likelihood ratio for this is

$$-2 \ln\left(\frac{\mathcal{L}_0}{\mathcal{L}(\xi S_{\mathrm{ref}})}\right) = \sum_{\mathrm{bins}}\left[2N \ln\left(1 + \frac{\xi S_{\mathrm{ref}}}{B}\right) - 2\xi S_{\mathrm{ref}}\right] \quad (13)$$

where we scale the number of expected signal counts from a source by a scale factor ξ and S_{ref} is the expected number of excess counts in a bin due to a DM source with a reference annihilation cross-section, $\langle \sigma_A v \rangle_{\mathrm{ref}}$ or decay lifetime, τ_{ref}. This allows us to calculate the decreasing likelihood of observing higher numbers of gamma-rays being emitted from a potential DM source. We find ξ such that

$$2.71 = TS + 2 \ln\left(\frac{\mathcal{L}_0}{\mathcal{L}(\xi S_{\mathrm{ref}})}\right). \quad (14)$$

For a one-sided 95% CL limit, the value of 2.71 corresponds to a likelihood which can be excluded at 95% CL.

Once the scale parameter ξ is found, we then scale the reference annihilation cross-section ($\langle \sigma_A v \rangle_{\mathrm{ref}}$) or decay lifetime ($\tau_{\mathrm{ref}}$) that was used to calculate the DM gamma-ray flux, for a given M_χ and annihilation channel, by the same parameter ξ. Thus our 95% CL limit on the annihilation cross-section becomes:

$$\langle \sigma_A v \rangle_{95\%} = \xi \times \langle \sigma_A v \rangle_{\mathrm{ref}} \quad (15)$$

and the limit on the decay lifetime is

$$\tau_{95\%} = \tau_{\mathrm{ref}} / \xi. \quad (16)$$

A.2. Joint Likelihood Analysis

For the joint likelihood analysis of many dSphs, the same likelihood analysis procedure is followed as described in the above section. However, now Equation (14) becomes

$$2.71 = \Delta TS = TS_{\mathrm{max}} - \sum_{\mathrm{bins}}\left[2N^{\mathrm{tot}} \ln\left(1 + \frac{\xi^{\mathrm{tot}} S_{\mathrm{ref}}^{\mathrm{tot}}}{B^{\mathrm{tot}}}\right) - 2\xi^{\mathrm{tot}} S_{\mathrm{ref}}^{\mathrm{tot}}\right] \quad (17)$$

where N^{tot} is the total events in each bin from data summed over all the dSphs, B^{tot} is the summed total of background counts from each dSph and $S_{\mathrm{ref}}^{\mathrm{tot}}$ is the total expected number of counts in each bin for the reference annihilation cross section or decay lifetime for all the dSphs. The same procedure is then followed: we find ξ^{tot} by imposing the condition in

Equation (17), such that the difference between TS_{max} and TS_{95} is equal to 2.71 for the combined analysis. Once ξ^{tot} is found, we can then scale $\langle \sigma_A v \rangle_{\mathrm{ref}}$ or τ_{ref} in order to set our constraint on the combined analysis of the dSphs:

$$\langle \sigma_A v \rangle_{95\%,\mathrm{Combined}} = \xi^{\mathrm{tot}} \times \langle \sigma_A v \rangle_{\mathrm{ref}} \quad (18)$$

$$\tau_{95\%,\mathrm{Combined}} = \tau_{\mathrm{ref}} / \xi^{\mathrm{tot}}. \quad (19)$$

Appendix B
Calculating Model Limits from Tabulated Flux Values

Although the interpretation of the limits in this paper is primarily DM focused, it cannot be stressed enough that, first and foremost, these are flux limits. As discussed in Section 4.3 and shown in Table 2, we have calculated generic flux limits for independent energy bins. In Table 2, we show the flux data which can be used to calculate these flux limits versus energy and can be used to constrain DM models. Here, we discuss how to use these flux limits to constrain DM models not considered in this paper.

The values in Table 2 are the best-fit flux and its uncertainty in each energy range for each source. Here, we discuss how to use these flux and error values to do a combined limit on any flux spectrum. The values in Table 2 give identical results to using these techniques for a single-energy-bin analysis.

For each energy bin i, let F_i^{fit} be the best-fit flux in that bin and ΔF_i be the error on the best-fit value. These are given in Table 2. Note that because there was no significant excess observed, many of these best-fit flux values are negative.

For a given DM model, select a reference value of $\langle \sigma_A v \rangle^{\mathrm{ref}}$ (for annihilation) or τ^{ref} (for decay). The limit will not depend on this choice of reference cross-section or lifetime, but it will be necessary for calculating flux in this calculation. For the flux spectrum to be constrained (F^{model}), define:

$$F_i^{\mathrm{model,ref}} \equiv F^{\mathrm{model}}(E_i; \langle \sigma_A v \rangle^{\mathrm{ref}}) \quad (20)$$

$$\mathrm{or}\ F_i^{\mathrm{model,ref}} \equiv F^{\mathrm{model}}(E_i; \tau^{\mathrm{ref}}) \quad (21)$$

depending on whether the calculation is for annihilation or decay. Here E_i is the energy of the bin i. Note that the final overflow bin for all energies above 56 TeV should not be used in this analysis because the bin energy is ill-defined. The calculated limit will be done as in Appendix A as

$$\langle \sigma_A v \rangle_{95\%} = \xi_{95} \times \langle \sigma_A v \rangle_{\mathrm{ref}} \quad (22)$$

$$\tau_{95\%} = \tau_{\mathrm{ref}} / \xi_{95}. \quad (23)$$

Because the test statistic TS follows a χ^2-distribution (given the caveats in Section 4.1), the best-fit values and errors in Table 2 can be interpreted as a χ^2 value. That is:

$$\chi_i^2 = \left(\frac{\xi F_i^{\mathrm{model,ref}} - F_i^{\mathrm{fit}}}{\Delta F_i}\right)^2 \quad (24)$$

for a single-energy bin for a single dSph.

These single-bin TS_i values can be summed over all energies to get a total constraint on the spectrum over all energies:

$$\chi^2 = \sum_i \left(\frac{\xi F_i^{\mathrm{model,ref}} - F_i^{\mathrm{fit}}}{\Delta F_i}\right)^2 \quad (25)$$

Similar to the TS calculation in Appendix A, we need to calculate the value of ξ which minimizes the χ^2. Because ξ

must be positive, fits to negative fluctuations correspond with $\xi = 0$, not $\xi < 0$. Define this minimum value of χ^2 as $\chi^2_{\min}$.

For a 95% CL limit on the spectrum, we need to find the value of ξ which gives $\mathrm{TS}^{\mathrm{tot}} = 2.71$. This can be done numerically, and the corresponding approximate 95% CL limits on the cross-section or lifetime are then calculated from Equation (22) or (23).

The calculation for ξ_{95} can also be calculated analytically. Define

$$A \equiv \sum_i \left(\frac{F_i^{\mathrm{model,ref}}}{\Delta F_i} \right)^2, \tag{26}$$

$$B \equiv \sum_i \left(\frac{F_i^{\mathrm{model,ref}} \times F_i^{\mathrm{fit}}}{(\Delta F_i)^2} \right), \tag{27}$$

$$C \equiv \sum_i \left(\frac{F_i^{\mathrm{fit}}}{\Delta F_i} \right)^2. \tag{28}$$

Then the χ^2 can be rewritten as

$$\chi^2 = \xi^2 A - 2\xi B + C. \tag{29}$$

Taking the derivative with respect to ξ gives us the value $\xi_{\min}$ which minimizes the χ^2

$$\xi_{\min} = \begin{cases} \frac{B}{A} & B \geqslant 0 \\ 0 & B \leqslant 0 \end{cases}. \tag{30}$$

In the case where $B \leqslant 0$, $\xi_{\min}$ is not allowed to go negative because it is typically assumed that there are no physical astrophysical sinks which produce negative flux, only positive sources. This corresponds with a minimum χ^2 value of

$$\chi^2_{\min} = \begin{cases} C - \frac{B^2}{A} & B \geqslant 0 \\ C & B \leqslant 0 \end{cases}. \tag{31}$$

The value of ξ which gives $\chi^2 - \chi^2_{\min} = 2.71$ is then

$$\chi^2 = 2.71 + \chi^2_{\min} = \xi_{95}^2 A - 2\xi_{95} B + C. \tag{32}$$

This is a simple quadratic equation, with solution

$$\xi_{95} = \frac{B + \sqrt{B^2 - A(C - \chi^2_{\min} - 2.71)}}{A}, \tag{33}$$

where we have taken the most positive root as the uppermost limit on ξ. Combining this with Equation (31), the value of ξ_{95} is

$$\xi_{95} = \begin{cases} \frac{B + \sqrt{2.71A}}{A} & B \geqslant 0 \\ \frac{B + \sqrt{B^2 + 2.71A}}{A} & B \leqslant 0 \end{cases}. \tag{34}$$

To calculate the combined limit from all dSphs, simply sum i over all energy bins of all sources, making sure to calculate $F_i^{\mathrm{model,ref}}$ for each source based on its J- or D-factor.

These limits have been checked over a variety of spectra and agree well with the full HAWC analysis calculation. It should be noted that the HAWC sensitivity depends on the spectrum of the gamma-ray source being studied, and the HAWC energy resolution is very broad. Additionally, although the statistical significance of these sources is roughly Gaussian and the statistical fluctuations are small, some calculation error is still introduced from these effects. Therefore, limits calculated in this way should be taken as approximate, particularly for spectra which peak strongly (such as gamma-ray lines). A more precise analysis of a candidate DM spectrum requires a full calculation through the HAWC analysis chain.

ORCID iDs

A. Albert ⓘ https://orcid.org/0000-0003-0197-5646
H. A. Ayala Solares ⓘ https://orcid.org/0000-0002-2084-5049
D. W. Fiorino ⓘ https://orcid.org/0000-0002-2302-9450
N. Fraija ⓘ https://orcid.org/0000-0002-0173-6453
V. Joshi ⓘ https://orcid.org/0000-0002-1457-4027
D. Kieda ⓘ https://orcid.org/0000-0003-4785-0101
R. J. Lauer ⓘ https://orcid.org/0000-0003-1933-7861
D. Lennarz ⓘ https://orcid.org/0000-0002-0614-7359
M. Mostafá ⓘ https://orcid.org/0000-0002-7675-4656
C. Rivière ⓘ https://orcid.org/0000-0002-0001-1581
D. Rosa-González ⓘ https://orcid.org/0000-0003-1327-0838
G. Vianello ⓘ https://orcid.org/0000-0002-2553-0839
S. Westerhoff ⓘ https://orcid.org/0000-0002-1422-7754
T. Yapici ⓘ https://orcid.org/0000-0002-5306-4804
H. Zhou ⓘ https://orcid.org/0000-0003-0513-3841

References

Aartsen, M., Abbasi, R., Abdou, Y., et al. 2013a, Sci, 342, 1242856
Aartsen, M., Abbasi, R., Abdou, Y., et al. 2013b, PhRvL, 111, 021103
Aartsen, M. G., Ackermann, M., Adams, J., et al. 2017, A&A, 607, A115
Abdo, A. A., Allen, B. T., Atkins, R., et al. 2012, ApJ, 750, 63
Abeysekara, A. U., Albert, A., Alfaro, R., et al. 2017, ApJ, 843, 39
Abeysekara, A. U., Alfaro, R., Alvarez, C., et al. 2014, PhRvD, 90, 122002
Abramowski, A., Aharonian, F., Ait Benkhali, F., et al. 2014, PhRvD, 90, 112012
Ackermann, M., Albert, A., Anderson, B., et al. 2014, PhRvD, 89, 042001
Ahnen, M. L., Ansoldi, S., Antonelli, L. A., et al. 2016, JCAP, 2016, 039
Aliu, E., Archambault, S., Arlen, T., et al. 2012, PhRvD, 85, 062001
An, H., Wise, M. B., & Zhang, Y. 2016, PhRvD, 93, 115020
Archambault, S., Archer, A., Benbow, W., et al. 2017, PhRvD, 95, 082001
Bai, Y., Lu, R., & Salvado, J. 2016, JHEP, 2016, 161
Baring, M. G., Ghosh, T., Queiroz, F. S., & Sinha, K. 2016, PhRvD, 93, 103009
Berlin, A., Hooper, D., & Krnjaic, G. 2016, PhLB, 760, 106
Bonnivard, V., Hütten, M., Nezri, E., et al. 2016, CoPhC, 200, 336
Boucenna, S. M., Chianese, M., Mangano, G., et al. 2015, JCAP, 1512, 055
Cholis, I., Dobler, G., Finkbeiner, D. P., Goodenough, L., & Weiner, N. 2009, PhRvD, 80, 123518
Esmaili, A., & Serpico, P. D. 2013, JCAP, 1311, 054
Feng, J. L., Kaplinghat, M., & Yu, H.-B. 2010, PhRvD, 82, 083525
Geringer-Sameth, A., Koushiappas, S. M., & Walker, M. 2015, ApJ, 801, 74
Harding, J. P. 2015, PoS, 236, 1227
Hayashi, K., Ichikawa, K., Matsumoto, S., et al. 2016, MNRAS, 461, 2914
Jungman, G., Kamionkowski, M., & Griest, K. 1996, PhR, 267, 195
Kopp, J., Liu, J., & Wang, X.-P. 2015, JHEP, 04, 105
Laevens, B. P. M., Martin, N. F., Ibata, R. A., et al. 2015, ApJL, 802, L18
Lattanzi, M., & Silk, J. 2009, PhRvD, 79, 083523
Navarro, J. F., Frenk, C. S., & White, S. D. M. 1997, ApJ, 490, 493
Navarro, J. F., Ludlow, A., Springel, V., et al. 2009, arXiv:0810.1522v2
Neyman, J., & Pearson, E. S. 1933, RSPTA, 231, 289
Patrignani, C., Agashe, K., Aielli, G., et al. 2016, ChPhC, 40, 100001
Protassov, R., van Dyk, D. A., Connors, A., Kashyap, V. L., & Siemiginowska, A. 2002, ApJ, 571, 545
Sjöstrand, T., Ask, S., Christiansen, J. R., et al. 2015, CoPhC, 191, 159
Sjöstrand, T., Mrenna, S., & Skands, P. Z. 2006, JHEP, 05, 026
Wilks, S. S. 1938, Ann. Math. Statist., 9, 60